



**HAL**  
open science

## Cu-Mn hydroxyapatite materials for toluene total oxidation

Maya Ibrahim, Madona Labaki, Nicolas Nuns, Jean-Marc Giraudon,  
Jean-Francois Lamonier

► **To cite this version:**

Maya Ibrahim, Madona Labaki, Nicolas Nuns, Jean-Marc Giraudon, Jean-Francois Lamonier. Cu-Mn hydroxyapatite materials for toluene total oxidation. ChemCatChem, 2019, ChemCatChem, 12 (2), pp.1-12. 10.1002/cctc.201901336 . hal-04285272

**HAL Id: hal-04285272**

**<https://hal.univ-lille.fr/hal-04285272v1>**

Submitted on 14 Nov 2023

**HAL** is a multi-disciplinary open access archive for the deposit and dissemination of scientific research documents, whether they are published or not. The documents may come from teaching and research institutions in France or abroad, or from public or private research centers.

L'archive ouverte pluridisciplinaire **HAL**, est destinée au dépôt et à la diffusion de documents scientifiques de niveau recherche, publiés ou non, émanant des établissements d'enseignement et de recherche français ou étrangers, des laboratoires publics ou privés.

# Cu-Mn hydroxyapatite materials for toluene total oxidation

Maya Ibrahim, <sup>[a,b]</sup> Madona Labaki, <sup>[b]</sup> Nicolas Nuns, <sup>[a]</sup> Jean-Marc Giraudon, <sup>\*[a]</sup> and Jean-François Lamonier <sup>[a]</sup>

- 
- [a] M. Ibrahim, N. Nuns, Dr. J.-M. Giraudon, Prof. J.-F. Lamonier  
Univ. Lille, CNRS, Centrale Lille, ENSCL, Univ. Artois, UMR 8181 - UCCS - Unité de Catalyse et Chimie du Solide, Lille, 59000, France  
E-mail : jean-marc.giraudon@univ-lille.fr
- [b] M. Ibrahim, Prof. M. Labaki  
Laboratory of Physical Chemistry of Materials (LCPM)/PR2N  
Lebanese University, Faculty of Sciences  
Fanar, BP 90656, Jdeidet El Metn (Lebanon)

Supporting information for this article is given via a link at the end of the document.

**Abstract:** The oxidation of 800 ppmv toluene in air has been investigated over  $\text{CuMnO}_x$  ((Cu + Mn) loading: 10 wt%) dispersed on hydroxyapatite (Hap:  $\text{Ca}_5(\text{PO}_4)_3(\text{OH})$ ) with different molar Cu/Mn compositions (2; 1; 0.5) to be compared with the corresponding supported single transition metal oxide catalysts. The solids have been prepared by wet aqueous co-impregnation method followed by a calcination at 400 °C for 4 h and physico-chemically characterized by different techniques. The catalytic performances of the supported Cu-Mn oxide catalysts revealed the existence of a synergetic effect in terms of activity and selectivity towards  $\text{CO}_2$  through the formation of Cu-Mn mixed oxides. The strongest synergetic effect is observed for a Cu/Mn molar ratio of 2 as confirmed by the standardised conversion rate values determined at 190 °C ( $r_{190}$ ) which followed the decreasing sequence ( $/10^{-2} \text{ h}^{-1}$ ):  $\text{Cu}_2\text{MnHap}$  (2.57) >  $\text{CuMnHap}$  (2.04) >  $\text{CuMn}_2\text{Hap}$  (1.59) >  $\text{MnHap}$  (1.13) >>  $\text{CuHap}$  (0.13). The highest activity of  $\text{Cu}_2\text{MnHap}$  can be explained by a better reducibility of the active phase in line with a high density of Cu-O-Mn interactions at the outermost layers as shown by ToF-SIMS results.

## Introduction

Volatile organic compounds (VOCs) are a large group of toxic chemicals that are easily released into the atmosphere, resulting in widespread environmental complications and negative health impacts. They are, therefore, recognized as the major contributors to air pollution. More stringent regulations have been adopted in order to control their release and reduce their daily emissions. Among the different VOC abatement techniques, total catalytic oxidation appears as an attractive technique. Indeed, this VOC treatment process is cost effective when compared to thermal incineration method due to operating conditions at much lower temperature and to high selectivity towards oxidation products such as  $\text{CO}_2$  and  $\text{H}_2\text{O}$  avoiding in that way undesirable by-products such as dioxins and nitrogen oxides.<sup>[1]</sup>

Although VOC total oxidation is generally performed over supported noble metals known for their high catalytic performances such as palladium and platinum <sup>[2-5]</sup> increasing studies focus nowadays on the use of cheaper transition metal oxides (TMO). Despite being generally less active than the noble metal based catalysts, they constitute a cost efficient alternative stability.<sup>[6-7]</sup> Furthermore, some metal oxides have demonstrated similar and even in some cases, slightly higher activity than that of noble metals. Indeed  $\gamma\text{-MnO}_2$  was found to be more active of Pt/ $\text{TiO}_2$  in toluene removal in specific conditions.<sup>[8]</sup> On the one hand, manganese oxides were found to exhibit great activity and selectivity in total oxidation of VOCs,<sup>[9,10]</sup> among which figures toluene <sup>[11]</sup> which is the target VOC to abate in this paper. On the other hand, copper oxides have also proven to be active and selective in the oxidation of toluene,<sup>[12]</sup> as well as good promoters for the removal of coke formed in the course of reaction.<sup>[13]</sup> Furthermore, a study conducted by Wang <sup>[14]</sup> on the complete oxidation of toluene revealed better catalytic performances for copper dispersed on alumina compared with other TM (Fe, Mn, Cr, Co, Mo, and Ni). Therefore, the use of a binary copper-manganese oxide can be an attractive strategy to improve the performance of the catalyst in the total oxidation of toluene. In that way, it has already been reported in the literature that bulk <sup>[15-20]</sup> and supported <sup>[16,21-24]</sup> Cu-Mn binary oxides can be considered as efficient catalysts in toluene oxidation, for which they exhibit higher catalytic activity than the single metal counterparts.

Important parameters such as the methods of synthesis, total TM loading, temperature of calcination, nature of the support, play key roles in tuning the optimized Cu/Mn ratio for the oxidation in toluene oxidation.

The good performances of Cu-Mn oxides in toluene oxidation have been reported to be due to segregated  $\text{CuO}/\gamma\text{-Mn}_2\text{O}_3$ , the presence of Cu allowing an enhanced catalytic activity of the manganese oxide for which active sites may be derived from the presence of  $\text{Mn}^{3+}$  in the near surface of the catalyst. <sup>[20]</sup> Other teams ascribed the enhanced catalytic activity to the formation of a mixed copper manganese oxide spinel phase allowing easier electron transfer between copper and

manganese cations. [16,21,22,24] Behar *et al.* reported on bulk  $\text{Cu}_{1.5}\text{Mn}_{1.5}\text{O}_4$  particles (10 nm) prepared from ionotropic alginate gel able to completely oxidize toluene at  $\approx 240$  °C. [16]

Cu-Mn binary oxides supported on conventional supports such as alumina, [23-25] titania, [16] and silica, [22] have been studied so far.

In the case of alumina supported Cu-Mn oxides, Saqer *et al.* [23] attributed the enhanced catalytic activity to the better dispersion of segregated  $\text{M}_x\text{O}_y$  (M = Cu, Mn) species, their increased reducibility (reactivity of surface oxygen), and their lower tendency to form coke deposits under reaction conditions. Li *et al.* [24] reported the best activity for a Cu/Mn atomic ratio of 1 on catalysts pretreated with  $\text{H}_2$  in line with the formation of the spinel phase  $\text{Cu}_{1.5}\text{Mn}_{1.5}\text{O}_4$ . However, it was found that the presence of water vapor had a negative effect on catalytic activity. Wang *et al.* [25] associated improved catalytic activity with the presence of highly dispersed Cu-O-Mn clusters in which part of the  $\text{Cu}^{2+}$  occupies the tetrahedral vacancies (TV) of alumina support, this strong interaction between Cu and Mn results in better redox properties. Considering titania, the Cu-Mn oxide supported on  $\text{TiO}_2$  obtained by incipient wetness impregnation shows an overall activity lower than for the unsupported  $\text{Cu}_{1.5}\text{Mn}_{1.5}\text{O}_4$ . [16]

Considering the silica based support, it was found that MCM-41-supported Cu-Mn oxide showed better activity than conventional amorphous silica,  $\beta$ -zeolite and ZSM-5-supported Cu-Mn catalysts. [22] It was supposed that highly dispersed Cu-Mn mixed oxides on mesoporous structure possibly provide active sites for the complete oxidation of toluene on the mesoporous catalysts.

The present work will focus on dispersing these active metal species on an unconventional support, which is hydroxyapatite (Hap). Hap is a material that has attracted much attention in numerous applications due to its non-toxicity, low cost, abundance in the natural environment, good chemical and thermal stability, high adsorption capacities when prepared through solution mediated synthesis. Furthermore, its characteristic properties, such as ionic exchange ability and tunable acid-base characteristics, [26-28] have been put forward to explain some catalytic activity differences in the VOC oxidation process. [29-34] In fact, a review on the use of hydroxyapatite as a multifunctional material for air, water and soil pollution control has been recently published. [35] Previous studies have aimed to study the effect of TM content on the performances of copper [36] and manganese [37,38] based active phases dispersed on Hap in the total oxidation of toluene to be correlated with the speciation and dispersion of the TM. For the TM-based Hap supported catalysts (TM = Cu, Mn), the maximum of activity is achieved for a low amount of Cu (wt%: 2.5 %) compared with those of 5-10 wt% for Mn.

With the objective to improve the catalyst efficiency, this study investigates the catalytic performances of Cu-Mn oxides dispersed on Hap in toluene oxidation considering a TM content of 10 wt% to be compared with those of the single supported TMO counterparts through the tuning of the Cu/Mn molar ratio. The catalytic performances will be correlated with the physico-chemical properties of the catalysts.

## Results and Discussion

### **Decomposition of the dried impregnated $\text{Cu}_x\text{Mn}_y\text{HapD}$ samples**

#### **Thermogravimetric analysis (TGA)**

The mode of decomposition of the dried impregnated samples ( $\text{Cu}_x\text{Mn}_y\text{HapD}$ ) was investigated using TGA technique and the resulting traces are given in Figure S2. The TGA traces (Figure S2-b) are rather similar for all samples. The first weight loss from 50 °C to 160 °C is ascribed to the departure of water. The second stage of decomposition which takes place in the temperature range of about 160-400 °C is attributed to the decomposition of  $\text{NO}_3^-$ . [39] It is found that the temperature of the large DTG peak (in °C) increases with Cu content owing to:  $\text{MnHapD}$  (190) <  $\text{Cu}_2\text{MnHapD}$  (300) <  $\text{CuHapD}$  (335) (Figure S2-b). Furthermore, based on the theoretical  $\text{NO}_3^-$  content in the Cu(II)/Mn(II) precursors and taking into account the  $\text{H}_2\text{O}$  removal contribution at low temperature, it is found that 82, 88 and 95 % of the initial nitrate content decompose for  $\text{CuHapD}$ ,  $\text{Cu}_2\text{MnHapD}$  and  $\text{MnHapD}$ , respectively. These results show that some remaining  $\text{NO}_3^-$  related species can be retained by the samples after calcinations performed at 400 °C for 4h.

#### **Structural, morphological and textural characterizations**

The X-ray diffractograms of the fresh  $\text{Cu}_x\text{Mn}_y\text{Hap}$  samples and of the Hap support are shown in Figure 1.

The characteristic peaks of Hap agree with those corresponding to the hexagonal phase  $\text{Ca}_5(\text{PO}_4)_3(\text{OH})$  (PDF 00-009-0432). It is found that the Full Width at Half Maximum (FWHM) for the (0 0 2) reflection is low as compared to the other ones in line with the presence of anisotropic crystallites as reported earlier in the literature. [26,40]

In Table 1 are listed two mean crystallite sizes obtained by the Scherrer equation from the FWHM of the peaks positioned at 10.9 ° and 25.9 ° relative to the (1 0 0) and (0 0 2) planes, respectively. This allows us to determine a length to thickness ratio of the crystallite through the determination of the  $D_{c(002)}/D_{c(100)}$  ratio which is of 1.81 for the Hap support. This ratio increases with the addition of Cu and/or Mn to get the highest value of 2.08 for  $\text{CuHap}$ . Thus, the addition of TM leads to slightly more elongated crystallite as compared to that of the Hap support as already observed by Chala *et al.* for  $\text{MnHap}$  samples. [38]

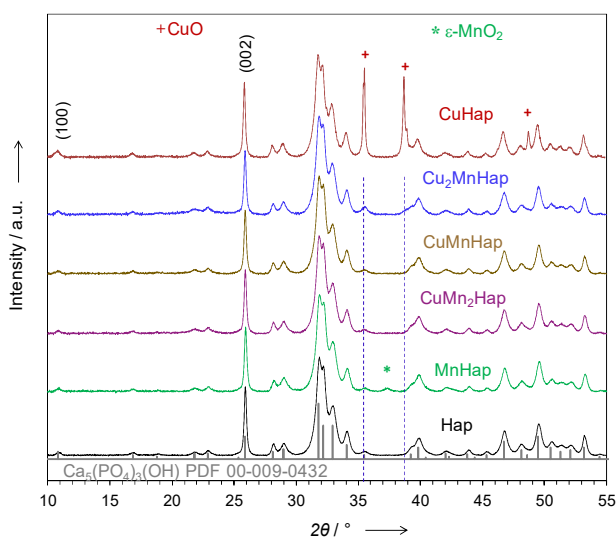


**Figure 1.** XRD patterns of pure Hap and  $\text{Cu}_x\text{Mn}_y\text{Hap}$  samples.

In addition to the characteristic peaks of Hap, we detect the presence of new peaks for the CuHap and MnHap solids. Indeed, the CuHap sample exhibits new peaks positioned at  $2\theta = 35.6^\circ$ ,  $38.8^\circ$  and  $48.8^\circ$  associated with monoclinic CuO tenorite (PDF No. 04-007-1375). The narrow sharp peaks are consistent with a mean crystallite size of 45 nm (see Table 1), in line with that of 42 nm reported by Chlala *et al.*,<sup>[36]</sup> indicating that the addition of copper on Hap by wet impregnation results in poor CuO dispersion for a 10 wt% of Cu.

**Table 1.** Mean crystallite size ( $D_c$ ) of Hap support and of TM related detected phases.

Sample	$D_{c(002)}$	$D_{c(100)}$	$D_{c(002)}/D_{c(100)}$	$D_c^{[a]}$	$D_c$
	[nm]	[nm]		[nm]	[nm]
	(002)	(100)	(002)/(100)		
Hap	36	20	1.81	-	-
CuHap	39	19	2.08	45	-
$\text{Cu}_2\text{MnHap}$	37	20	1.85	-	-
CuMnHap	37	18	1.99	-	-
$\text{CuMn}_2\text{Hap}$	38	21	1.81	-	-
MnHap	35	18	1.90	-	16

<sup>[a]</sup> : determined from the peak at  $2\theta = 48.8^\circ$

The X-ray diffractogram of MnHap shows a new distinct broad peak located at  $2\theta = 37.1^\circ$  which can be tentatively attributed to the akhtenskite  $\epsilon\text{-MnO}_2$  (PDF n° 00-030-0820) phase (Figure S1) which was not previously detected in similar conditions<sup>[37]</sup>.

Regarding the binary oxide materials, for the Cu-rich sample, we observe an increase in intensity and broadness of the peak located at  $2\theta = 35.5^\circ$  and of the shoulder at  $2\theta = 38.7^\circ$ . However, the broadness of the peaks precludes discriminating a CuO from a related Cu-Mn spinel phase as shown in Figure 2.

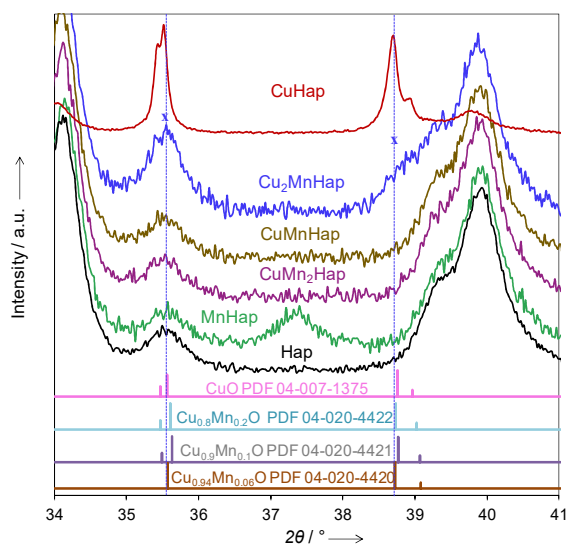


**Figure 2.** X-ray diffractograms of the  $\text{Cu}_x\text{Mn}_y\text{Hap}$  solids in the  $2\theta = 34\text{--}41^\circ$  range. The intensity of the diffractogram of CuHap was divided by 10.

By opposition, for the enriched Mn samples, *i.e.* CuMnHap and CuMn<sub>2</sub>Hap, we do not observe any additional peaks to those of the pure Hap, which could be explained either by a high dispersion of the TMO phase(s) or/and by the formation of supported amorphous TMO phase(s).

**Table 2.** Textural properties and H<sub>2</sub>-TPR results.

Sample	SSA <sup>[a]</sup> [m <sup>2</sup> .g <sup>-1</sup> ]	V <sub>p</sub> <sup>[b]</sup> [cm <sup>3</sup> .g <sup>-1</sup> ]	n(H <sub>2</sub> ) <sub>th</sub> <sup>[c]</sup> [mmol.g <sup>-1</sup> ]	n(H <sub>2</sub> ) <sub>ex</sub> <sup>[d]</sup> [mmol.g <sup>-1</sup> ]
Hap	102	0.70	-	-
CuHap	71	0.46	5.51 (1.58)	4.96
Cu <sub>2</sub> MnHap	78	0.49	2.67 (1.65)	1.99
CuMnHap	79	0.54	1.83 (1.69)	1.19
CuMn <sub>2</sub> Hap	86	0.56	1.46 (1.73)	0.98
MnHap	78	0.51	1.78 (1.82)	0.67

[a] Specific surface area. [b] Pore volume. [c] Experimental amount of H<sub>2</sub> consumed on the fresh catalysts; Theoretical amount of H<sub>2</sub> consumed (see text).

[d] Experimental amount of H<sub>2</sub> consumed on the used catalysts.

The anisotropy observed by XRD was also evidenced through SEM analysis (Figure 3). Indeed, some bundles of fiber-like particles are observed for all our samples, indicating an anisotropic growth of the particles with a length varying from 50 nm to almost 400 nm for all samples.

The main textural properties of the samples are summarized in Table 2. The Hap support has a specific surface area of 102 m<sup>2</sup>.g<sup>-1</sup> and a pore volume of 0.70 cm<sup>3</sup>.g<sup>-1</sup>. When adding Cu and/or Mn, both the BET surface area and pore volume values decrease. This decrease is higher in the case of CuHap, due most probably to some pore blockage by CuO particles.

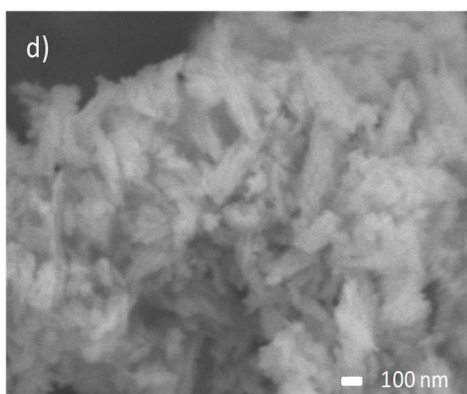
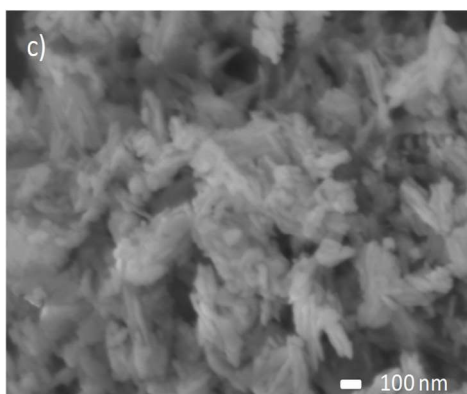
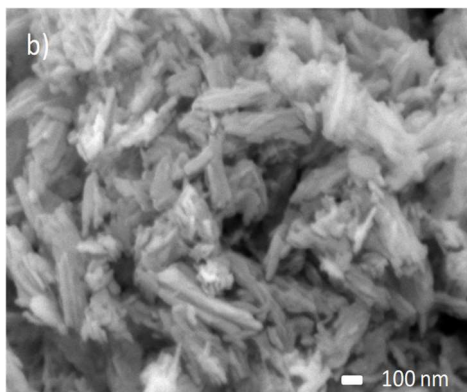
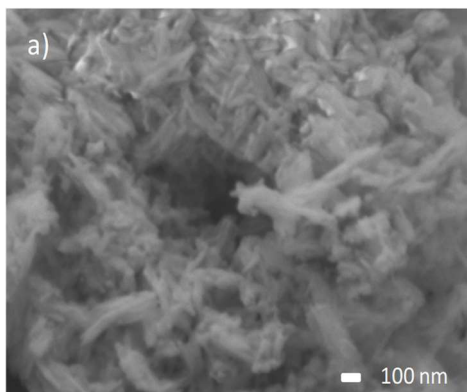


**Figure 3.** SEM images of a) Hap, b) CuHap, c) CuMnHap and d) MnHap.

***Redox characterization***

***Temperature programmed reduction ( $H_2$ -TPR) coupled with mass spectrometry (MS)***

The H<sub>2</sub>-TPR profiles of the calcined materials are illustrated in Figure S3 and the quantitative results are reported in Table 2. As expected the pure apatitic support does not exhibit any reduction peak (not shown here).<sup>[41,42]</sup> For MnHap one peak of H<sub>2</sub> consumption at 370 °C was observed, followed by a tail. The trace relative to CuHap is complex showing at high temperature a strong H<sub>2</sub> consumption due to overlapping peaks at 452 °C and 485 °C while a low temperature H<sub>2</sub>-consumption is also observed. By opposition the H<sub>2</sub>-TPR profiles of the Cu-Mn based materials show only two overlapping peaks in a narrow temperature range. Interestingly, the onset of H<sub>2</sub> consumption decreases while the peak enlargement increases with the increase of Cu content.

The experimental H<sub>2</sub> consumptions expressed per g of catalyst  $n(\text{H}_2)_{\text{ex}}$  increase with Cu content from 1.46 (CuMn<sub>2</sub>Hap) to 5.51 (CuHap). These values were compared to the theoretical ones  $n(\text{H}_2)_{\text{th}}$  regarded as maximum values assuming Cu(+II) → Cu(0) and Mn(+IV) → Mn(II) reductions. We noticed that  $n(\text{H}_2)_{\text{ex}}$  exceeds  $n(\text{H}_2)_{\text{th}}$  for Cu/Mn atomic ratio  $\geq 1.0$ . This can be explained by taking into account that some reducible NO<sub>3</sub><sup>-</sup> related entities are retained in the materials after calcination. This assumption is supported by the FT-IR results exhibiting the characteristic unreacted nitrate band at 1386 cm<sup>-1</sup> whose relative intensity increases with Cu content (not shown here) as already observed by Chlala *et al.*<sup>[36]</sup>

On purpose, the degradation modes of the NO<sub>3</sub><sup>-</sup> species have been monitored using mass spectroscopy through the evolution of *m/z* signals 17, 28, 30 and 44 characteristic of NH<sub>3</sub>, N<sub>2</sub>, NO and N<sub>2</sub>O as a function of temperature (Figure S4). For the Cu-Mn based catalysts the evolution of these *m/z* signals over time are rather similar. A peak of high intensity at *m/z* = 30 is observed, followed by a narrow less intense peak at *m/z* = 28 while the contributions at *m/z* = 17 and 44 are negligible. Hence, during the H<sub>2</sub>-TPR experiments it turns out that the NO<sub>3</sub><sup>-</sup> entities are reduced into NO then into N<sub>2</sub> while the contributions of gaseous N<sub>2</sub>O and NH<sub>3</sub> appear to be negligible. Such scheme of NO<sub>3</sub><sup>-</sup> degradation holds also for the MnHap sample. However, in that case the relative contribution of N<sub>2</sub> is less pronounced.

Taking into account the ability of Cu(0) to efficiently reduce the nitrate entities at low temperature, the T<sub>NO</sub> value has been taken as a reference to describe the reducibility of the materials: the easier the reducibility of the materials, the lower T<sub>NO</sub> is. Thereby, as seen in Figure 4 the solids can be ranked according to the decreasing temperature of NO appearance T<sub>NO</sub> (°C): Cu<sub>2</sub>MnHap (174) < CuMnHap (188) < CuHap (200) < CuMn<sub>2</sub>Hap (212) < MnHap (236). For the Cu-Mn related catalysts it turns out that T<sub>NO</sub> decreases with an increase of Cu content showing that high relative Cu content promotes the reducibility of the materials. It should also be noted that T<sub>NO</sub> is lower for Cu/Mn = 2 and 1 as compared to those relative to the single TM based catalyst.

Additionally, the H<sub>2</sub>-TPR profile of the fresh Cu-Mn based catalysts exhibits a typical profile similar to those of mixed Cu-Mn oxides<sup>[43-44]</sup> in line with the co-impregnation method.

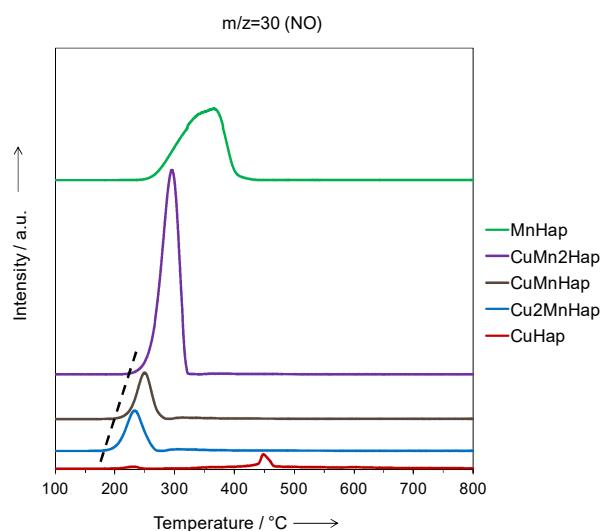


**Figure 4.** Evolution of the *m/z* = 30 (NO) signal for the Cu<sub>x</sub>Mn<sub>y</sub>Hap solids.

## Surface characterizations

### XPS results

Figure 5 gives the Cu 2p core level XPS spectra for the fresh samples and the pertinent results are given in Table 3 and S2. The Cu 2p<sub>3/2</sub> binding energy (BE) for CuHap is at 932.8 ± 0.1 eV considering the first and second recorded XPS spectra while the FWHM decreases from 3.4 eV to 2.7 eV. By opposition, for all the Cu<sub>x</sub>Mn<sub>y</sub>Hap samples, the Cu 2p<sub>3/2</sub> BEs are much higher, located at 934.1 ± 0.1 eV with FWHM of 3.2 ± 0.3 eV and I<sub>sat</sub>/I<sub>pp</sub> ratio about twice higher than that of CuHap, in line with a Cu(II). However, considering the second Cu 2p XPS, it is observed for all samples a significant Cu

2p<sub>3/2</sub> BE decrease accompanied with a decrease of FWHM and I<sub>sat</sub>/I<sub>pp</sub> ratio. Based on all these observations, it is concluded that XPS induces reduction of copper at different extents as already observed.<sup>[36]</sup> Copper is significantly reduced on CuHap considering the first XPS spectra, while a partial copper reduction is observed for the Cu<sub>x</sub>Mn<sub>y</sub>Hap samples regarding the second recording XPS spectra. Such different behaviors in terms of copper reduction can be tentatively ascribed to the presence of a mixed CuMn oxide which stabilizes the Cu towards XPS photons.

**Table 3.** XPS based data obtained for the fresh and used catalysts.

Sample	Cu 2p <sub>3/2</sub> <sup>[a]</sup>	FWHM Cu 2p <sub>3/2</sub> <sup>[a]</sup>	I <sub>sat</sub> /I <sub>pp</sub> <sup>[a]</sup>	Mn AOS <sup>[b]</sup>	Mn/Cu
CuHap	932.8	3.42	0.38	-	-
Cu <sub>2</sub> MnHap	933.9	3.40	0.60	2.6	1.1
CuMnHap	934.0	3.50	0.65	2.6	2.0
CuMn <sub>2</sub> Hap	934.4	3.04	0.69	2.7	5.3
MnHap	-	-	-	3.1	-
CuHapU	933.3	4.20	0.44	-	-
Cu <sub>2</sub> MnHapU	933.7	3.66	0.51	2.0	1.1
CuMnHapU	934.2	3.20	0.55	2.0	2.3
CuMn <sub>2</sub> HapU	934.4	4.14	0.62	2.3	5.1
MnHapU	-	-	-	2.5	-

[a] Data obtained for 1<sup>st</sup> recording. [b] Mn average oxidation state.

The Mn 3s core levels for the Mn containing samples have been investigated. From the splitting between the two multiplet spin components a Mn average oxidation state (AOS) has been estimated which gives a value of 3.1 for MnHap while those for Cu<sub>x</sub>Mn<sub>y</sub>Hap decrease to 2.7-2.6.

The Mn/Cu atomic ratio compared to the nominal Mn/Cu shows a Mn surface enrichment which becomes more pronounced with increasing Mn content.

### **Time of Flight Secondary Ions Mass Spectrometry (ToF-SIMS)**

Regarding the Hap support, the peaks displayed in the positive ToF-SIMS spectra include Ca<sup>+</sup> (m/z = 40), CaH<sup>+</sup> (m/z = 41), CaO<sup>+</sup> (m/z = 56), CaOH<sup>+</sup> (m/z = 57) and Ca<sub>2</sub>O<sup>+</sup> (m/z = 96), Ca<sub>2</sub>PO<sub>3</sub><sup>+</sup> (m/z = 159), Ca<sub>2</sub>PO<sub>4</sub><sup>+</sup> (m/z = 175), CaPO<sub>3</sub>H<sup>+</sup> (m/z = 120), CaPO<sub>4</sub>H<sub>2</sub><sup>+</sup> (m/z = 137), Ca<sub>2</sub>PO<sub>3</sub>H<sup>+</sup> (m/z = 160), Ca<sub>3</sub>P<sub>2</sub>O<sub>3</sub>H<sup>+</sup> (m/z = 231), Ca<sub>4</sub>P<sub>2</sub>O<sub>4</sub>H<sup>+</sup> (m/z = 287), Ca<sub>5</sub>P<sub>2</sub>O<sub>5</sub>H<sup>+</sup> (m/z = 343) and Ca<sub>5</sub>(PO<sub>4</sub>)<sub>3</sub><sup>+</sup> (m/z = 485) which are the characteristic secondary ions observed for Ca<sub>5</sub>(PO<sub>4</sub>)<sub>3</sub>(OH).<sup>[45-49]</sup> In the negative polarity, O<sup>-</sup> (m/z = 16), HO<sup>-</sup> (m/z = 17), P<sup>-</sup> (m/z = 31), PO<sup>-</sup> (m/z = 47), PO<sub>2</sub><sup>-</sup> (m/z = 63), and PO<sub>3</sub><sup>-</sup> (m/z = 79) are found. It should be mentioned that some mineral impurities such as Na<sup>+</sup> (m/z = 23), Mg<sup>+</sup> (m/z = 24), K<sup>+</sup> (m/z = 39) and some hydrocarbons C<sub>x</sub>H<sub>y</sub>O<sub>z</sub><sup>+</sup> were detected as well. Additionally all samples exhibit the NO<sup>-</sup> (m/z = 30), NO<sub>2</sub><sup>-</sup> (m/z = 46) and NO<sub>3</sub><sup>-</sup> (m/z = 62) secondary ions in line with residual nitrate after calcination.

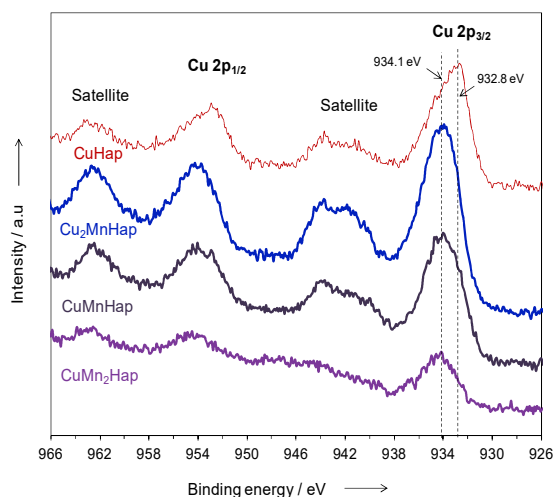


**Figure 5.1**<sup>st</sup> recording of the Cu 2p XPS core levels.

The existence of interactions between the TM and hydroxyapatite in TMHap (TM = Cu or Mn) materials is evidenced by the presence of a series of cluster ions involving TM and Ca or P and both (see Table S3, S4, 4). Based on these results, it is found that Cu and Mn preferentially interact with Ca rather than P. This statement has already been reported in the case of Hap supported Mn samples by Chlala *et al.*<sup>[37]</sup> These observations suggest the occurrence of an ion (Ca-Cu/Mn) exchange at the outermost layers of the samples.

**Table 4.** List of ToF-SIMS positive secondary ions detected in Cu-Mn based solids

$\text{Cu}_x\text{Mn}_y\text{Ca}_z\text{O}_2\text{H}_w^+$	$\text{Cu}_x\text{Mn}_y\text{P}_i\text{O}_2\text{H}_w^+$	$\text{Cu}_x\text{Mn}_y\text{Ca}_z\text{P}_i\text{O}_2\text{H}_w^+$	$\text{Cu}_x\text{Mn}_y\text{O}_2\text{H}_w^+$
n.d. <sup>[a]</sup>	CuMnPH	n.d. <sup>[a]</sup>	CuMn
	CuMnPH <sub>2</sub>		<sup>65</sup> CuMn
	<sup>65</sup> CuMnPH <sub>2</sub>		CuMnO
			<sup>65</sup> CuMnO
			CuMnOH
			<sup>65</sup> CuMnOH

[a] Not detected.

Interestingly for the CuMn based samples, the ToF-SIMS spectra in positive polarity exhibit a series of mixed  $\text{Cu}_x\text{Mn}_y\text{O}_2\text{H}_w^+$  ( $x = 1; y = 1; z = 0, 1; w = 0-2$ ) ions (see Table 4).

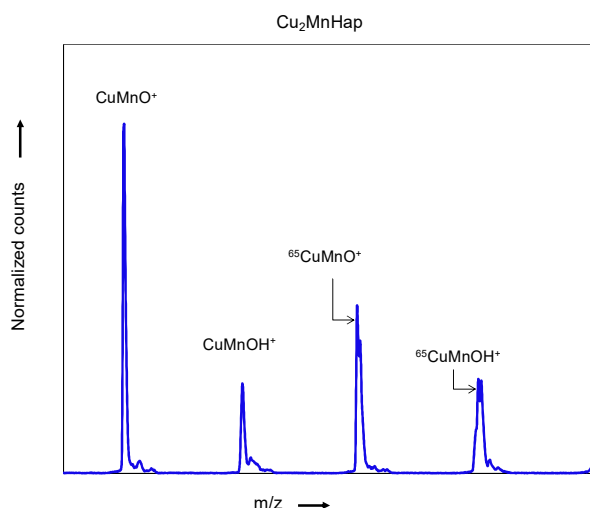


**Figure 6.** ToF-SIMS (+) spectrum in the  $m/z$  133–138 range collected from the  $\text{Cu}_2\text{MnHap}$  sample.

For example the ToF-SIMS (+) spectrum of  $\text{Cu}_2\text{MnHap}$  in the  $m/z$  133-138 range displayed in Figure 6 evidences the  $\text{CuMnO}^+$  and  $\text{CuMnOH}^+$  secondary ions. The presence of such ions proves the formation of mixed Cu-O-Mn oxide. However, it is not possible to identify the mixed oxide phase just based on the ToF-SIMS fragmentation patterns. In parallel, in order to evaluate the relative surface density of Cu-O-Mn interactions the ToF-SIMS intensity ratio  $\text{CuMnO}^+ / (\text{Cu}^+ + \text{Mn}^+)$  for the  $\text{Cu}_x\text{Mn}_y\text{Hap}$  solids has been determined. This allows to classify the catalysts by decreasing intensity ratio to get the following sequence:  $\text{Cu}_2\text{MnHap}$  (0.057) >  $\text{CuMnHap}$  (0.040) >  $\text{CuMn}_2\text{Hap}$  (0.025). This result highlights the greater contribution of Cu-O-Mn interactions for  $\text{Cu}_2\text{MnHap}$ .

#### **Catalytic oxidation of toluene**

The conversion of toluene into  $\text{CO}_2$  over Hap and  $\text{Cu}_x\text{Mn}_y\text{Hap}$  catalysts as a function of temperature is given in Figure 7. It should be noted that the toluene conversion is significantly enhanced by the addition of single TM with good redox properties over the hydroxyapatite support. Additionally, the catalysts perform even better when adding Cu and Mn on the support by co-impregnation. Toluene conversion into  $\text{CO}_2$  based on  $T_{50}(\text{CO}_2)$  (temperature at which 50 % of toluene is converted into  $\text{CO}_2$  in  $^\circ\text{C}$ ) decreases in the following order:  $\text{Cu}_2\text{MnHap}$  (196) >  $\text{CuMnHap}$  (202)  $\approx$   $\text{CuMn}_2\text{Hap}$  (205) >  $\text{MnHap}$  (210)  $\gg$   $\text{CuHap}$  (255). 90 % of toluene conversion was achieved for  $\text{CuHap}$  and  $\text{MnHap}$  at temperatures of 302  $^\circ\text{C}$  and 224  $^\circ\text{C}$ , respectively, while a temperature below 220  $^\circ\text{C}$  was required for Cu-Mn based catalysts. Indeed, the same order of decreasing activity was maintained for all catalysts for both  $T_{90}(\text{CO}_2)$  and  $T_{10}(\text{CO}_2)$  (see Table S5). Considering a standardised conversion rate determined at 190  $^\circ\text{C}$  ( $r_{190}$ ), the catalysts can be ranked by decreasing activity ( $/10^{-2} \text{ h}^{-1}$ ) following the same previous sequence:  $\text{Cu}_2\text{MnHap}$  (2.57) >  $\text{CuMnHap}$  (2.04) >  $\text{CuMn}_2\text{Hap}$  (1.59) >  $\text{MnHap}$  (1.13)  $\gg$   $\text{CuHap}$  (0.13). It should be noted that  $r_{190}$  for  $\text{Cu}_2\text{MnHap}$  catalyst is 2 times higher and 20 times higher compared to those obtained with  $\text{MnHap}$  and  $\text{CuHap}$ , respectively.

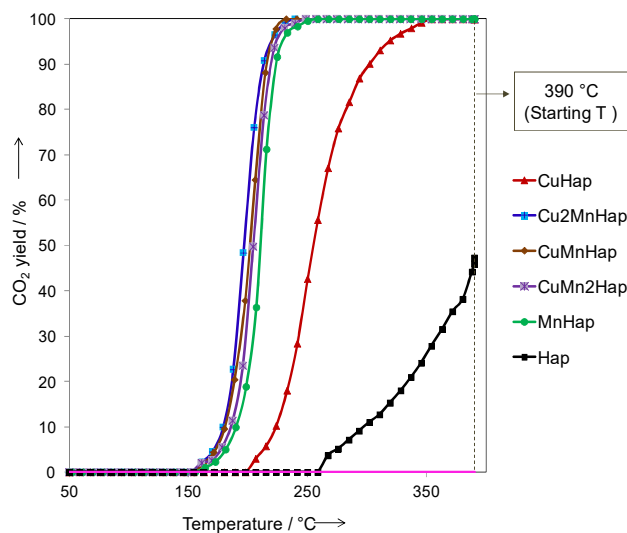


**Figure 7.** CO<sub>2</sub> yield for Cu<sub>x</sub>Mn<sub>y</sub>Hap catalysts (GHSV = 14,500 h<sup>-1</sup>; 800 ppmv toluene in air).

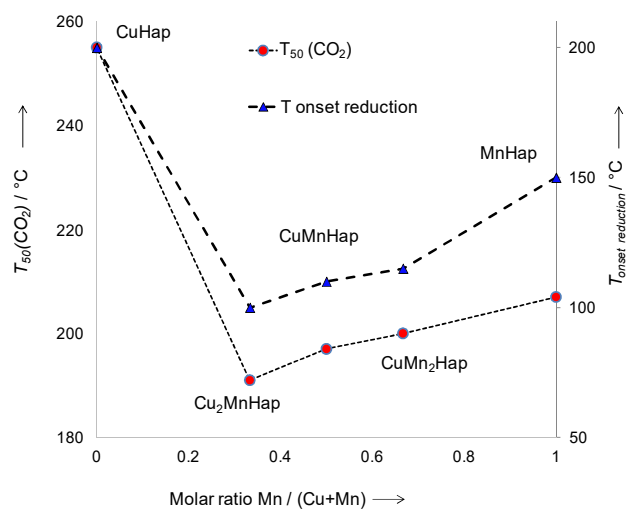


**Figure 8.** T<sub>50</sub> (CO<sub>2</sub>) (left axis) and T<sub>onset reduction</sub> (right axis) vs. Mn/(Cu+Mn) molar ratio.

T<sub>50</sub> (CO<sub>2</sub>) as a function of the Mn/(Cu+Mn) molar ratio (Figure 8) shows a parabolic resembling curve indicating a better activity in terms of specific activity for the supported mixed oxides. It should be noted that the specific activity is the highest for a Cu/Mn ratio of 2.0. Moreover, the production of CO is lower over Cu-Mn based catalysts as compared to those of the single

TMHap samples, to become non-detectable over the Cu<sub>2</sub>MnHap sample (Figure S5) in line with previous studies showing a better activity for CO oxidation into CO<sub>2</sub> for such Cu/Mn stoichiometry. [50-51] Figure 8 clearly shows a nice correlation between the catalytic activity in terms of T<sub>50</sub>(CO<sub>2</sub>) and the reducibility of the catalysts in terms of the onset reduction temperature (T<sub>or</sub>). This correlation highlights the importance of the redox behaviour of the catalysts for such reaction.

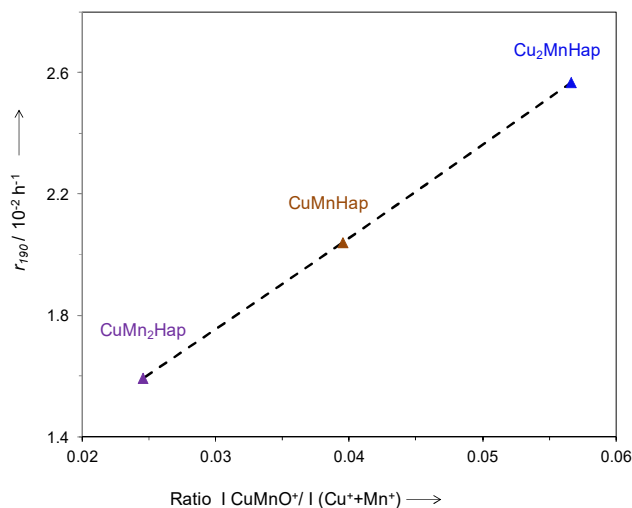


**Figure 9.**  $r_{190}$  as a function of  $\text{CuMnO}^+ / \text{Cu}^+ + \text{Mn}^+$  intensity ratio for the mixed  $\text{Cu}_x\text{Mn}_y\text{Hap}$  catalysts.

Interestingly, as shown in figure 9, the standardised rate  $r_{190}$  increases linearly with the  $\text{CuMnO}^+ / (\text{Cu}^+ + \text{Mn}^+)$  ToF-SIMS intensity ratio. It is recognized that the formation of Cu-O-Mn entities, in which the polar covalent Mn-O bond is weakened by the presence of Cu, promotes oxygen lability.<sup>[52-53]</sup> Furthermore, the electron transfer between copper and manganese cations is made easier.

### Stability tests

Stability tests of  $\text{Cu}_x\text{Mn}_y\text{Hap}$  catalysts were conducted at 200 °C in similar conditions to those of the catalytic tests. As can be seen in Figure 10, a decrease in toluene conversion is noted for all  $\text{Cu}_x\text{Mn}_y\text{Hap}$  catalysts. A quantification of the deactivation resistance of our catalysts was performed through the use of an activity coefficient  $a_{200}$  determined by calculating the ratio of toluene conversion after 24 h of test to that obtained at the beginning of the test. The evolution of the values of  $a_{200}$  as a function of Mn/(Cu+Mn) molar ratio is given in Figure 11. Therefore, the used catalysts can be ranked by decreasing resistance towards deactivation:  $\text{CuHap} \gg \text{MnHap} > \text{Cu}_2\text{MnHap} \approx \text{CuMnHap} \approx \text{CuMn}_2\text{Hap}$ .

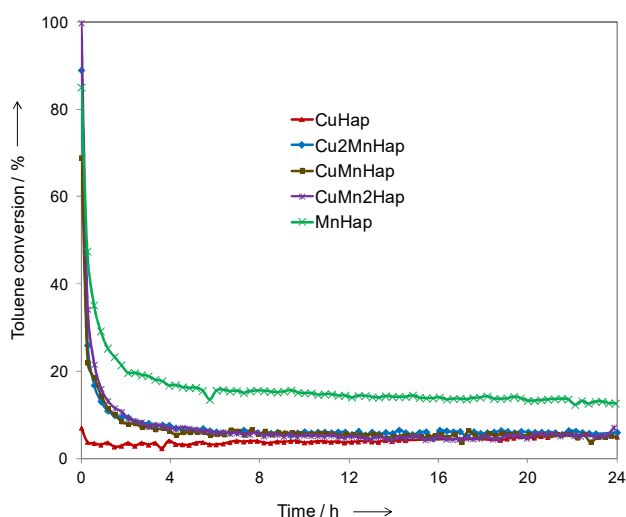


**Figure 10.** Time course for toluene oxidation over  $\text{Cu}_x\text{Mn}_y\text{Hap}$  catalysts activated at 200 °C. Feed composition: 800 ppmv toluene in air,  $T_{\text{test}} = 200$  °C

The effect of the temperature of activation was investigated in the case of CuMnHap. Increasing the temperature from 200 °C to 390 °C allows to quadruple the toluene conversion which amounts now to 18 % as observed in Figure 12.

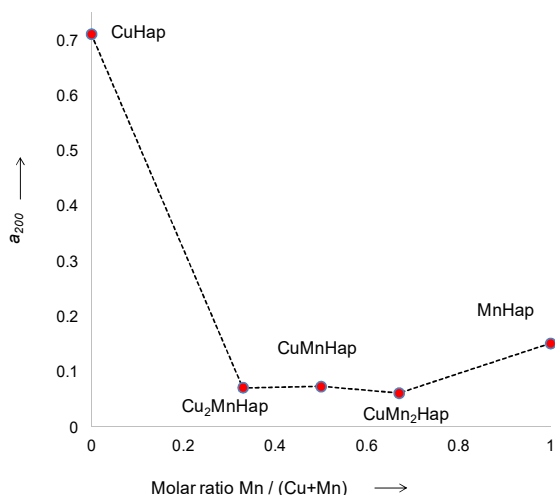


**Figure 11.** Evolution of activity coefficient  $a_{200}$  as a function of Mn/(Cu+Mn) molar ratio.

### Characterisations after stability tests

In order to get insight about the deactivation, additional characterizations have been performed on the used catalysts. The XRD patterns of the Cu<sub>x</sub>Mn<sub>y</sub>HapU samples reveal no modification in the positions and relative intensities of the peaks previously observed in fresh samples, nor does it reveal any new crystalline phase.

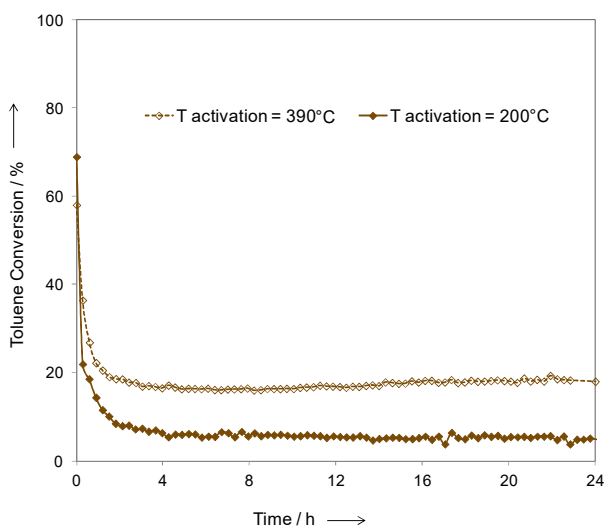


**Figure 12.** Time course for toluene oxidation over CuMnHap catalyst activated either at 200 °C or 390 °C. Feed composition: 800 ppmv toluene in air,  $T_{\text{test}} = 200$  °C.

By opposition the reducibility of the used catalysts is significantly altered compared to that of the fresh catalysts in terms of H<sub>2</sub>-TPR profiles as shown in Figure 13 and in terms of H<sub>2</sub> consumption amount (Table 2). For the CuHapU and Cu<sub>2</sub>MnHapU samples it is found that  $n(\text{H}_2)_{\text{ex}}$  is higher than  $n(\text{H}_2)_{\text{th}}$  indicating that NO<sub>3</sub><sup>-</sup> related moieties are still incorporated in the catalysts. For the MnHapU sample is found a very complex H<sub>2</sub>-TPR trace showing at least five overlapping contributions. Furthermore, the H<sub>2</sub> consumption amount is low and results in a Mn AOS of 2.7 highlighting the reduction of the MnO<sub>x</sub> species. For the used CuMn based catalysts, it is found that the onset reduction temperature is all the lower when the Cu content is higher, as previously observed for the fresh samples. All the traces are initially composed of an intense narrow peak followed by a complex tail constituted of overlapping components in a wide temperature window (up to 700 °C). Furthermore, a global H<sub>2</sub>-consumption decrease is noted compared to that observed on the fresh samples, which becomes all the more pronounced the higher the Mn content is.

Interestingly, it should be noticed that the amount of H<sub>2</sub>-TPR consumed for the low temperature peak corresponds to the total conversion of Cu(II) into Cu(0) within the margin of uncertainty (see Table 5). As a consequence, the H<sub>2</sub>-TPR profiles of these two CuMn based catalysts consist in the successive reductions of Cu(II) into Cu(0) and of Mn<sup>x+</sup> into Mn(II). Taking into account the remaining amount of H<sub>2</sub> consumed in the TPR experiments, a Mn AOS of 2.8 and 2.6 has been estimated for the CuMnHapU and CuMn<sub>2</sub>HapU samples, respectively. Therefore, the Mn entities appear more reduced after the stability test as previously noticed.<sup>[38]</sup> The total oxidation of toluene over Cu-Mn mixed oxide can be described by a Mars-van Krevelen model in which the toluene is oxidized by the catalyst and the gaseous dioxygen restore the oxidized state of the catalyst. Taking this model into account, the Mn reoxidation can be herein the rate limiting step of the process. A possible decomposition of the mixed Cu<sub>x</sub>Mn<sub>y</sub>O<sub>z</sub> species present in fresh Cu-Mn samples into CuO and MnO<sub>x</sub> after catalytic reaction could account for such a behaviour.

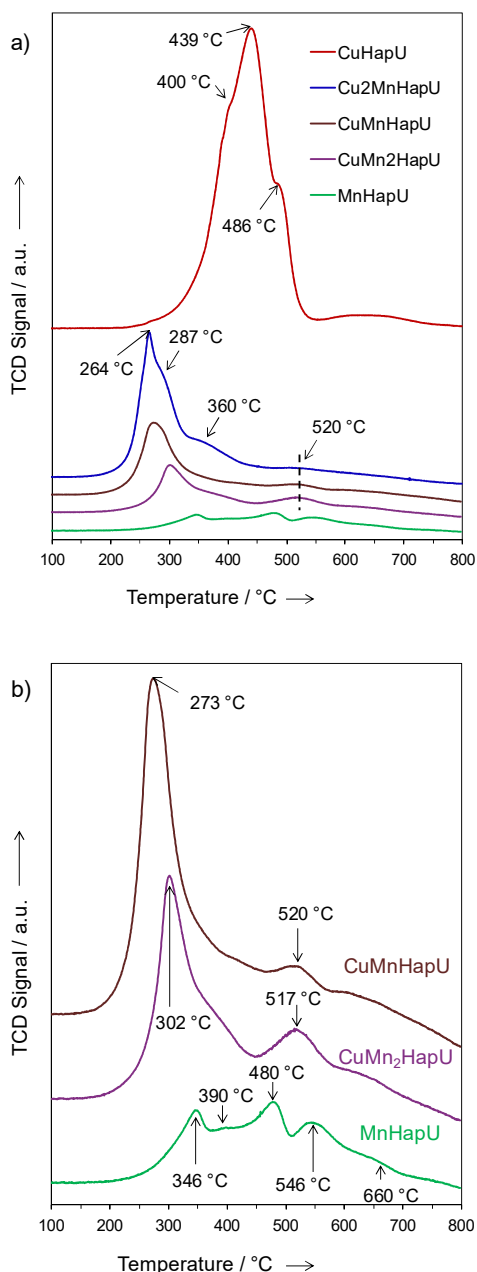


**Figure 13.** (a) H<sub>2</sub>-TPR reduction profiles for Cu<sub>x</sub>Mn<sub>y</sub>HapU solids and b) zoom of the H<sub>2</sub>-TPR reduction profiles for CuMnHapU, CuMn<sub>2</sub>HapU and MnHapU.

This assumption is in line with the work of Papavasiliou *et al.*<sup>[54]</sup> In this study the performances of Cu–Mn spinel oxide materials were investigated in steam reforming of methanol. A decomposition of the spinel was noted following the catalytic

reaction. It was claimed that the difficulty in oxidizing Mn(II) leads to the spinel decomposition. To conclude, such a similar behaviour may have likely occurred in our experiments.

**Table 5.** H<sub>2</sub> consumption amounts and Mn AOS

Sample	n(H <sub>2</sub> ) <sub>th</sub> [a] [mmol.g <sup>-1</sup> ]	n(H <sub>2</sub> ) <sub>ex</sub> [b] [mmol.g <sup>-1</sup> ]	Mn AOS [c]
CuMnHapU	0.84	0.84	2.8
CuMn <sub>2</sub> HapU	0.58	0.65	2.6
MnHapU	-	-	2.7

[a] Theoretical amount of H<sub>2</sub> consumed corresponding to the reduction of CuO to Cu<sup>0</sup>. [b] Experimental amount of H<sub>2</sub> consumed relative to the low temperature reduction peak considered as symmetric. [c] Manganese average oxidation state.

Cu 2p core level XPS spectra for the used samples that are illustrated in Figure S6 show that the copper state is still (+II) for the supported Cu-Mn oxides (Table 3). By opposition the Mn AOS decreases after durability test (Table 3) while the Mn/Cu atomic ratios remain practically unchanged.

## Conclusion

Hydroxyapatite supported binary Cu-Mn (TM: 10 wt%) oxides with different atomic Cu/Mn composition (2; 1; 0.5), were successfully synthesized by co-impregnation and calcined at 400 °C for 4 h. The performances of these catalysts were compared to those of the single TM in the catalytic oxidation of toluene in dry air. Adding Cu to Mn promotes in any case the total oxidation of toluene into CO<sub>2</sub> with the highest activity and CO<sub>2</sub> selectivity obtained for the catalyst having a Cu/Mn molar ratio of 2. These improved catalytic performances could be correlated with improved reducibility induced by the presence of supported a mixed copper-manganese phase. However, the catalysts deactivate with time. Such a deactivation of Hap supported Cu-Mn based oxides with time may be explained by a decomposition of the mixed entities.

## Experimental Section

### Material preparation

#### *Synthesis of the Stoichiometric Hap support*

Stoichiometric hydroxyapatite, with a Ca/P molar ratio of 1.67, was prepared by a co-precipitation technique. [26] 150 mL of an aqueous solution of Ca(NO<sub>3</sub>)<sub>2</sub>·4H<sub>2</sub>O (0.0835 mole, Riedel-de Haën, purity ≥ 98%) was added dropwise to 500 mL of a NH<sub>4</sub>H<sub>2</sub>PO<sub>4</sub> solution (0.05 mole, Fluka; purity ≥ 99%) under stirring at pH 10 (by properly adding ammonia (25%; Scharlau) to the reaction media) under reflux to give a white precipitate. The maturation duration was 1 h under constant stirring. After filtration, washing with hot deionized water and drying (80 °C for 18 h) a calcination step was performed in dry air (400 °C for 4 h, 2 °C.min<sup>-1</sup>) to get the Hap support.

#### *Synthesis of the catalysts (10 wt% of TM)*

CuHap: In a typical experiment 1.76 g of Cu(NO<sub>3</sub>)<sub>2</sub>·3H<sub>2</sub>O (Sigma Aldrich, purity ≥ 99%), was dissolved in 50 mL of deionized water and the apatitic support (4.0 g) was then added. The pH of the Cu(II) nitrate aqueous solution (50 mL) was 4.0. This pH turned out to be 4.6 when the Hap support (solid) was added to the Cu(II) solution (50 mL). Rotary evaporation (Büchi Rotavapor R-114; 60 °C; 20 rpm; 70 mbar) was used to remove water. After 30 min of evaporation (volume of the solution: 35 mL) the pH decreased to 4.3 to keep stable after further evaporation of the solution. The recovered powder was dried and calcined in similar conditions to those relative to the Hap support. MnHap: the synthesis was carried in a similar way as for CuHap using Mn(NO<sub>3</sub>)<sub>2</sub>·4H<sub>2</sub>O (Sigma Aldrich purity ≥ 97%) as Mn(II) precursor. The CuMn<sub>2</sub>Hap, CuMnHap and Cu<sub>2</sub>MnHap samples (Cu/Mn molar ratio: 0.5 ; 1 ; 2) were synthesized by dissolving the suitable Cu(II) and Mn(II) precursors in 50 mL of deionized water and subsequently treated in a similar manner to before. The weight percentages of Cu and Mn were 3.66% and 6.34%, 5.36 % and 4.64 %, 6.98 % and 3.02 % for CuMn<sub>2</sub>Hap, CuMnHap, and Cu<sub>2</sub>MnHap, respectively.

### Characterization

#### *X-ray diffraction (XRD)*

XRD studies were carried out using a Bruker AXS D8 Advance powder diffractometer equipped with a LynxEye Super Speed detector and a Cu-K $\alpha$  radiation ( $\lambda = 1.5418 \text{ \AA}$ ), operating in the  $10^\circ \leq 2\theta \leq 55^\circ$  range with a step of  $0.02^\circ$  and a count time of 5 s. The identification of the crystalline phases present in a sample was accomplished by comparing the registered patterns with the ICDD PDF-4 database cards, processed on EVA software. Furthermore, the mean crystallite size of the Hap supported Cu and/or Mn oxide catalysts, was determined by the Scherrer equation corrected from the line broadening of the apparatus using LaB $_6$  as an internal reference.

### ***N<sub>2</sub> physisorption analysis***

Nitrogen absorption-desorption measurements were conducted with a Micromeritics Tristar II Surface Areas and Porosity apparatus. The specific surface areas were calculated according to the BET (Brunauer, Emmet and Teller) method, based on the evaluation of the quantity of physisorbed N $_2$ , whereas, pore volume and size distribution were determined by the BJH (Barrett, Joyner and Halenda) method. Prior to data collection, each sample ( $\approx 500 \text{ mg}$ ) was outgassed under vacuum at  $200^\circ \text{C}$  for 2 h.

### ***Scanning electron microscopy***

Scanning electron micrographs were recorded on a JEOL JSM 7500F operating at an accelerating voltage of 5 kV. Prior to analysis, a thin chromium coating was performed on the samples in order to reduce potential charging effect.

### ***Thermogravimetric analysis (TGA)***

Thermogravimetric analysis (TGA) was carried out using a TA Balance instrument, model: SDT 2960 DSC-TGA X, under a flow of 20 % O $_2$  in helium ( $100 \text{ mL}\cdot\text{min}^{-1}$ ), going from room temperature to  $600^\circ \text{C}$  with a heating rate of  $5^\circ \text{C}\cdot\text{min}^{-1}$ .

### ***Infrared spectroscopy (IR)***

FTIR (Fourier transform infrared) spectra were recorded at room temperature, under vacuum, in a spectral range spanning from 200 to  $4000 \text{ cm}^{-1}$ , while using a Nicolet 460 spectrometer. These spectra were an average of 256 scans with a spectral resolution of  $4 \text{ cm}^{-1}$ . Thin, disk-shaped pellets of the catalysts were prepared by compressing 30 mg of an intimate mixture, composed of 1 mg of powdered sample combined with 100 mg of dried KBr. A spectrum of an empty cell was first recorded. This spectrum served as a background spectrum, which would be subsequently subtracted from that of the samples analyzed.

### ***X-ray photoelectron spectroscopy (XPS)***

XPS measurements were carried out on an AXIS Ultra DLD Kratos spectrometer, that employs a monochromatic Al-K $\alpha$  source ( $h\nu = 1486.6 \text{ eV}$ ), operating at 120 W. The X-ray photoelectron spectra were recorded at ambient temperature, while using an ultra-high vacuum system (base pressure:  $10^{-9} \text{ mbar}$ ). All binding energies were calibrated with respect to adventitious carbon C 1s peak BE located at 284.8 eV. Data processing was performed using CasaXPS software. The average oxidation state (AOS) of Mn was calculated, based on the magnitude of the Mn 3s multiplet splitting. XPS spectra of Cu 2p core level were recorded twice: at the beginning and at the end of XPS analysis. XPS quantification of Cu was performed according to the method described in the work of Ye *et al.* [15]

### ***Temperature programmed reduction (H<sub>2</sub>-TPR) coupled with mass spectrometry (MS)***

The H $_2$ -TPR experiments were carried out on a Micromeritics Autochem II (2920) instrument, equipped with a U-shaped quartz reactor. Temperature-programmed reduction experiments were performed on the fresh (200 mg) and used catalysts (100 mg) previously cleaned in Ar at  $150^\circ \text{C}$  for 1 h. After cooling down the samples were flushed with 5 vol% H $_2$ /Ar gaseous mixture ( $50 \text{ mL}\cdot\text{min}^{-1}$ ) from  $25^\circ \text{C}$  to  $800^\circ \text{C}$  ( $10^\circ \text{C}\cdot\text{min}^{-1}$ ). The monitoring of hydrogen consumption was performed by a thermal conductivity detector (TCD). A cold trap, composed of isopropanol and liquid nitrogen, was used to remove water from the gas before the detector. The quantification of the amount of H $_2$  consumed was accomplished by integration of the H $_2$ -TPR profiles. The H $_2$ -TPR analysis was coupled with mass spectrometry (MS), able to identify, through the study of m/z signals, the various produced gaseous molecules at the exit of the reactor.

### ***Time of Flight Secondary Ion Mass Spectrometry (ToF-SIMS)***

Positive and negative Time-of-Flight Secondary Ion Mass Spectrometry (ToF-SIMS) measurements were performed with a TOF-SIMS $^5$  spectrometer (ION-TOF GmbH Germany) equipped with a bismuth liquid metal ion gun (LMIG). The compacted samples were bombarded with pulsed Bi $^{3+}$  primary ion beam (25 keV, 0.25 pA) rastered over a  $500 \times 500 \mu\text{m}^2$  surface area. With a data acquisition of 100 s, the total fluence does not amount up to  $10^{12} \text{ ions}\cdot\text{cm}^{-2}$  ensuring static conditions. Charge effects were compensated by means of a 20 eV pulsed electron flood gun. In these experiments, the mass resolution ( $m/\Delta m$ ) was about 3200 at  $m/z = 175$  for Ca $_2$ PO $_4^+$ . The secondary ions were identified by their exact mass, coupled with the appropriate intensities for the expected isotope pattern.

### ***Catalytic tests***

The catalytic tests were carried out in a continuous-flow fixed-bed Pyrex reactor, with 200 mg of catalyst, under atmospheric pressure. The reactor was set in an electric furnace, and the reaction temperature was continuously monitored by two thermocouples, one attached to the outside of the reactor and one inserted into a thermowell, placed in the middle of the catalyst bed. The reactive gas mixture consisted of 800 ppmv of toluene diluted in dry air ( $100 \text{ mL}\cdot\text{min}^{-1}$ ) corresponding to a gas hourly space velocity (GHSV) of  $14,500 \text{ h}^{-1}$ .

The catalysts were activated in air at 390 °C for 2 h (75 mL.min<sup>-1</sup>) then submitted to the reactive mixture for 1 h before to decrease the temperature from 390 °C to 25 °C at a rate of 0.5 °C.min<sup>-1</sup>. The gaseous products were analyzed quantitatively by gas chromatograph (7860A Agilent Gas Chromatograph) equipped with two detectors and two columns: a Thermal Conductivity Detector (TCD) that identifies permanent gases (CO, CO<sub>2</sub>, etc.), separated on a Restek Shin Carbon ST/Silco HP NOC 80/100 micro packed column; and a Flame Ionization Detector (FID) that recognizes hydrocarbons and aromatic compounds (toluene, benzene, etc.), separated on a capillary column CP-Wax 52 CB: 25 m, Ø 0.25 mm × 1.2 µm.

Toluene conversion (C<sub>t</sub>) was assessed according to the following formula:

$$C_t (\%) = \frac{[\text{toluene}]_i - [\text{toluene}]_t}{[\text{toluene}]_i} \times 100 \quad \text{Equation (1)}$$

where [toluene]<sub>i</sub> and [toluene]<sub>t</sub> were respectively toluene inlet and outlet concentrations.

The yield in CO<sub>2</sub> was determined by the equation below:

$$C_{\text{CO}_2} (\%) = \frac{[\text{CO}_2]_t \times 100}{7 \times [\text{toluene}]_i} \quad \text{Equation (2)}$$

where [CO<sub>2</sub>]<sub>t</sub> was the CO<sub>2</sub> outlet concentration.

The standardised rate of toluene conversion r<sub>190</sub> expressed in mole of reacted toluene per hour and per mol of TM, was evaluated as follows:

$$r = \frac{\text{ppmTol} \times F_T \times C_t}{V_m \times n_{\text{TM}}} \quad \text{Equation (3)}$$

where F<sub>T</sub> was the total volumetric flow rate, C<sub>t</sub> the toluene conversion at 190 °C, V<sub>m</sub> the molar volume equal to 24.4 L.mol<sup>-1</sup> and n<sub>TM</sub> the total amount of TM. After activation of the catalysts at 200 °C for 2 h in air flow (75 mL.min<sup>-1</sup>) the stability tests were performed at 200 °C for 24 h following the same experimental procedure exposed before. The used catalysts were labelled with the suffix U.

## Acknowledgements

The “DepollutAir” project (grant number 1.1.18) of the European Program INTERREG V France-Wallonie-Flanders (FEDER), Chevreur institute (FR 2638), Ministère de l’Enseignement Supérieur et de la Recherche and Région Hauts-de-France are acknowledged for the funding and their support for this work. This research has also been partially supported by a French–Lebanese research project (PHC CEDRE N°32933QE), a grant from the Lebanese CNRS 2016–2017 project N°01-08-15, a PhD grant from the Lebanese University and ARCUS E2D2 project.

**Keywords:** Catalytic oxidation • Toluene • Copper • Manganese • Hydroxyapatite

- [1] J.-F. Lamonier, *Catalysts* 2016, 6, 7.
- [2] M. Hosseini, T. Barakat, R. Cousin, A. Aboukaïs, B. L. Su, G. De Weireld, S. Siffert, *Appl. Catal. B Environ.* 2012, 111, 218–224.
- [3] J. Bedia, J. M. Rosas, J. Rodríguez-Mirasol, T. Cordero, *Appl. Catal. B Environ.* 2010, 94, 8–18.
- [4] V. P. Santos, S. A. Carabineiro, P. B. Tavares, M. F. Pereira, J. J. Órfão, J. L. Figueiredo, *Appl. Catal. B Environ.* 2010, 99, 198–205.
- [5] L. F. Liotta, *Appl. Catal. B Environ.* 2010, 100, 403–412.
- [6] W. B. Li, J. X. Wang, H. Gong, *Catal. Today* 2009, 148, 81–87.
- [7] W. Tang, G. Liu, D. Li, H. Liu, X. Wu, N. Han, Y. Chen, *Sci. China Chem.* 2015, 58, 1359–1366.
- [8] C. Lahousse, A. Bernier, P. Grange, B. Delmon, P. Papaefthimiou, T. Ioannides, X. Verykios, *J. Catal.* 1998, 178, 214–225.
- [9] M. Piumetti, D. Fino, N. Russo, *Appl. Catal. B Environ.* 2015, 163, 277–287.
- [10] J. Q. Torres, J.-M. Giraudon, J.-F. Lamonier, *Catal. Today* 2011, 176, 277–280.
- [11] Y. Peng, L. Zhang, L. Chen, D. Yuan, G. Wang, X. Meng, F.-S. Xiao, *Catal. Today* 2017, 297, 182–187.
- [12] D. Romero, D. Chlala, M. Labaki, S. Royer, J.-P. Bellat, I. Bezverkhy, J.-M. Giraudon, J.-F. Lamonier, *Catalysts* 2015, 5, 1479–1497.
- [13] A. P. Antunes, M. F. Ribeiro, J. M. Silva, F. R. Ribeiro, P. Magnoux, M. Guisnet, *Appl. Catal. B Environ.* 2001, 33, 149–164.
- [14] C.-H. Wang, *Chemosphere* 2004, 55, 11–17.
- [15] Z. Ye, J.-M. Giraudon, N. Nuns, P. Simon, N. De Geyter, R. Morent, J.-F. Lamonier, *Appl. Catal. B Environ.* 2018, 223, 154–166.
- [16] S. Behar, P. Gonzalez, P. Agulhon, F. Quignard, D. Świerczyński, *Catal. Today* 2012, 189, 35–41.
- [17] J. Hu, W. B. Li, R. F. Liu, *Catal. Today* 2018, 314, 147–153.
- [18] Y. Liu, L. Jia, Y. Lin, Y. Zhao, L. Sun, H. Ma, H. Kameyama, M. Sakurai, Y. Guo, *J. Chem. Eng. Jpn.* 2018, 51, 769–777.
- [19] D. A. Aguilera, A. Perez, R. Molina, S. Moreno, *Appl. Catal. B Environ.* 2011, 104, 144–150.
- [20] H. C. Genuino, S. Dharmarathna, E. C. Njagi, M. C. Mei, S. L. Suib, *J. Phys. Chem. C* 2012, 116, 12066–12078.
- [21] H. J. Kim, S. W. Choi, C. S. Lee, B. Wielage, S. Bae, S. O. Obare, H. I. Inyang, *Environ. Eng. Sci.* 2011, 28, 827–833.
- [22] W. B. Li, M. Zhuang, T. C. Xiao, M. L. H. Green, *J. Phys. Chem. B* 2006, 110, 21568–21571.
- [23] S. M. Saqer, D. I. Kondarides, X. E. Verykios, *Appl. Catal. B Environ.* 2011, 103, 275–286.
- [24] X. Li, L. Wang, Q. Xia, Z. Liu, Z. Li, *Catal. Commun.* 2011, 14, 15–19.
- [25] H. Wang, Y. Lu, Y. Han, C. Lu, H. Wan, Z. Xu, S. Zheng, *Appl. Surf. Sci.* 2017, 420, 260–266.
- [26] L. Silvester, J.-F. Lamonier, R.-N. Vannier, C. Lamonier, M. Capron, A.-S. Mamede, F. Pourpoint, A. Gervasini, F. Dumeignil, *J. Mater. Chem. A* 2014, 2, 11073–11090.

- [27] S. Diallo-Garcia, M. B. Osman, J.-M. Krafft, S. Casale, C. Thomas, J. Kubo, G. Costentin, *J. Phys. Chem. C* 2014, 118, 12744–12757.
- [28] N. S. Resende, M. Nele, V. M. Salim, *Thermochim. Acta* 2006, 451, 16–21.
- [29] H. Nishikawa, T. Oka, N. Asai, H. Simomichi, T. Shirai, M. Fuji, *Appl. Surf. Sci.* 2012, 258, 5370–5374.
- [30] C. Lamonier, J.-F. Lamonier, B. Aellach, A. Ezzamarty, J. Leglise, *Catal. Today* 2011, 164, 124–130.
- [31] H. Monma, *J. Catal.* 1982, 75, 200–203.
- [32] C. L. Kibby, W. K. Hall, *J. Catal.* 1973, 31, 65–73.
- [33] Y. Matsumura, J. B. Moffat, *J. Chem. Soc. Faraday Trans.* 1996, 92, 1981–1984.
- [34] W. T. Reichle, *J. Catal.* 1970, 17, 297–305.
- [35] M. Ibrahim, M. Labaki, J.-M. Giraudon, J.-F. Lamonier, *J. Hazard. Mater.* 2020, 383, 121139.
- [36] D. Chlala, J.-M. Giraudon, N. Nuns, M. Labaki, J.-F. Lamonier, *ChemCatChem* 2017, 9, 2275–2283.
- [37] D. Chlala, A. Griboval-Constant, N. Nuns, J.-M. Giraudon, M. Labaki, J.-F. Lamonier, *Catal. Today* 2018, 307, 41–47.
- [38] D. Chlala, J.-M. Giraudon, N. Nuns, C. Lancelot, R.-N. Vannier, M. Labaki, J.-F. Lamonier, *Appl. Catal. B Environ.* 2016, 184, 87–95.
- [39] D. Chlala, PhD Thesis, University of Lille, 2015.
- [40] B. Maaten, J. Moussa, C. Desmaretz, P. Gredin, P. Beaunier, T. Kanger, K. Tönsuaadu, D. Villemin, M. Gruselle, *J. Mol. Catal. Chem.* 2014, 393, 112–116.
- [41] Z. Qu, Y. Sun, D. Chen, Y. Wang, *J. Mol. Catal. Chem.* 2014, 393, 182–190.
- [42] C. Wen, Y. Cui, X. Chen, B. Zong, W.-L. Dai, *Appl. Catal. B Environ.* 2015, 162, 483–493.
- [43] F. C. Buciuman, F. Patcas, T. Hahn, *Chem. Eng. Process.* 1999, 38, 563–569.
- [44] V. H. Vu, J. Belkouch, A. Ould-Dris, B. Taouk, *AIChE J.* 2008, 54, 1585–1591.
- [45] H. B. Lu, C. T. Campbell, D. J. Graham, B. D. Ratner, *Anal. Chem.* 2000, 72, 2886–2894.
- [46] R. França, T. D. Samani, G. Bayade, L. Yahia, E. Sacher, *J. Colloid Interface Sci.* 2014, 420, 182–188.
- [47] R. Oriňaková, A. Oriňak, M. Kupková, M. Hrubovčáková, L. Škantárová, A. Turoňová, L. M. Bučková, C. Muhmann, H. M. Arlinghaus, *Int. J. Electrochem. Sci.* 2015, 10, 659–670.
- [48] S. R. Leadley, M. C. Davies, C. C. Ribeiro, M. A. Barbosa, A. J. Paul, J. F. Watts, *Biomaterials* 1997, 18, 311–316.
- [49] M. J. Ziglo, A. E. Nelson, G. Heo, P. W. Major, *Appl. Surf. Sci.* 2009, 255, 6790–6794.
- [50] E. C. Njagi, C.-H. Chen, H. Genuino, H. Galindo, H. Huang, S. L. Suib, *Appl. Catal. B Environ.* 2010, 99, 103–110.
- [51] L. Shi, Z.-H. Hu, G.-M. Deng, W.-C. Li, *Chin. J. Catal.* 2015, 36, 1920–1927.
- [52] W. Y. Hernández, M. A. Centeno, F. Romero-Sarria, S. Ivanova, M. Montes, J. A. Odriozola, *Catal. Today* 2010, 157, 160–165.
- [53] W. Y. Hernández, M. A. Centeno, S. Ivanova, P. Eloy, E. M. Gaigneaux, J. A. Odriozola, *Appl. Catal. B Environ.* 2012, 123, 27–35.
- [54] J. Papavasiliou, G. Avgouropoulos, T. Ioannides, *J. Catal.* 2007, 251, 7–20.